Fuel 241 (2019) 1117–1128

Contents lists available at ScienceDirect

Fuel

journal homepage: www.elsevier.com/locate/fuel

Full Length Article

Surfactant flooding in oil-wet micromodels with high permeability fractures

Lucas Mejia[a], Mohsen Tagavifar[b,1], Ke Xu[c,1], Miguel Mejia[a], Yujing Du[a], Matthew Balhoff[a,*]

[a] The University of Texas at Austin, United States
[b] Chevron Corporation, Houston, TX, United States
[c] Massachusetts Institute of Technology, Cambridge, MA, United States

ARTICLE INFO

Keywords:
Micromodel
Surfactant
EOR
Fractured
Oil-wet
Viscous crossflow

ABSTRACT

Recovery in carbonate reservoirs is challenging because they are often oil wet and highly fractured. Surfactant flooding has been proposed as a possible enhanced oil recovery method to address these problems. To better understand the mechanisms of oil recovery from oil-wet, fractured rocks using surfactants, we created oil-wet glass micromodels, traversed by a deep fracture (130 μm) and conducted surfactant spontaneous imbibition experiments and floods at typical reservoir flow rates (approximately 2 ft/day). We compared the effects of capillary, viscous, and gravity forces as well as wettability alteration. We show, by conducting spontaneous imbibition experiments with negligible gravity effects (inverse Bond number $\sim 10^5$) and by analyzing the results using simple force balance calculations, that in our micromodels low IFT plays the key role in balancing the viscous, gravity, and surface forces and hence the dynamics of imbibition. To quantify the role of viscous forces, we present displacement experiments at low IFT (10^{-3} mN/m) where transverse viscous pressure gradients mobilize oil from the matrix into the fracture. These results help rationalize and quantify the contributions of gravity, wettability alteration, and viscous crossflow to the rate of matrix-fracture transfer at low-IFT conditions.

1. Introduction

Carbonates hold approximately 40–60% of the world's oil reserves [1]. Most of these rocks are naturally fractured and oil-wet [2,3]. If the natural fractures are highly interconnected and the matrix-fracture permeability contrast is high, secondary and tertiary oil recovery processes are challenging to implement because injected aqueous fluids flow from the injector to the producer primarily through the connected fracture network, with limited imbibition into the rock matrix that contains most of the hydrocarbons. Surfactants have been proposed and used as enhanced oil recovery (EOR) agents in fractured oil-wet reservoirs because they can lower interfacial tension and alter wettability from oil-wetting to water-wetting.

Surfactant solutions can desaturate oil from cores in static imbibition cells. Standnes and Austad [4] used cationic and anionic surfactants to quantify oil recovery from a low permeability chalk in an imbibition cell and concluded that recovery was a result of wettability alteration or low interfacial tension. Zhang et al. [5] used surfactant-alkali mixtures to modify wettability of a marble plate with a corrugated surface and decrease interfacial tension between oil and water for the idealized case of oil trapped between two plates. Their study showed an alkali-surfactant bath successfully recovered oil from a marble plate-glass slit while a water bath did not. Additionally, separate imbibition studies in Texas Cordova cream limestone cores identified wettability alteration and low interfacial tension as the mechanisms of oil production[6,7]. We intend to complement these experiments with visualizations of transfer mechanisms in order to better understand how oil can be recovered from fractured carbonates.

Dynamic effects seem to increase the efficiency of oil production by surfactant flooding. Simulations carried out using a chemical flooding reservoir simulator showed that injecting viscous fluid at low IFT into a fracture that is adjacent to a block of matrix results in oil desaturation from the matrix [8]. Additionally, coreflooding experiments, where surfactant solution was injected into a fractured core, showed that flow through the fracture increased the rate of oil recovery compared to static imbibition experiments [9], and that increasing microemulsion viscosity also increased the rate of recovery [10]. Some of the experiments presented here elaborate on how oil is mobilized from the fracture to the matrix under dynamic conditions. Floods in our micromodels show transverse flow is an important recovery mechanism for fractured carbonates undergoing surfactant flooding.

Even though corefloods are valuable tools for EOR screening, it is challenging to visualize multiphase flow in the core's pore space [11–13]. Microfluidic systems can be designed to model a rock with an

* Corresponding author.
E-mail address: balhoff@mail.utexas.edu (M. Balhoff).
[1] Work conducted while at UT Austin.

https://doi.org/10.1016/j.fuel.2018.12.076
Received 11 October 2018; Received in revised form 12 December 2018; Accepted 13 December 2018

arbitrary geometry; micromodels have been widely used to study different EOR methods [14–20]. Additionally, experiments in fractured micromodels with disconnected fractures have been conducted observing water-air and water-oil displacements [21,22]. Fundamental studies pertaining to the formation and dynamics of microemulsion [13] and to the wettability alteration of initially oil-wet pores by surfactant solution [23,24] have provided insight into the time scales at which these processes happen at idealized conditions. We take advantage of the flexibility in the fabrication of micromodels to design a platform that has the two characteristics that make carbonates difficult to produce using EOR: oil-wetting solid surfaces and inclusion of very high permeability fractures. By observing surfactant floods in our oil-wet, fractured micromodels we directly visualize matrix-fracture transfer of phases and provide direct evidence of wettability alteration of the solid. These phenomena are of interest for EOR in carbonates as different mechanisms (wettability alteration, viscous crossflow, solubilization) have been proposed as dominant at specific recovery conditions (namely spontaneous imbibition versus imposed flow) [4,5,8].

Micromodel experiments investigating surfactant or alkali-surfactant-polymer flooding are reported in the literature [25–30], but none in micromodels where the fracture network connects the inlet and outlet ports, as in this study. These projects provided insight into the mechanisms of surfactant and ASP flooding, but did not delve on the effect of low IFT flooding in fractured media. Such a subset of conditions (fractured, oil-wet) are important to consider as they tend to hinder success of EOR processes in carbonates. A goal in EOR operations in carbonates is mobilizing the oil in the rock matrix to the fractures so that it can flow to producing wells. We examine the performance of surfactant flooding in micromodels where very high permeability fractures connect inlet and outlet ports because such micromodels are a simple representation of the type II fractured carbonate reservoirs described by Nelson (2001). Using our fractured micromodel, we can directly identify some of the ways oil is mobilized from the matrix.

2. Experimental

2.1. Fluids

A light crude oil (density = 0.88 g/cm^3, molecular weight = 263 g/mol, viscosity = 13.6 mPa.s) with an acid number of 0.05 ± 0.02 (mg KOH/g) was used in all experiments. Oil was filtered through a 0.45 μm filter paper before use. Deionized water was obtained from a Millipore Direct-Q 5, with a minimal resistivity of 18.2 MΩ·cm. The surfactants tridecyl alcohol propoxy Sulfate (C_{13}-13PO-SO_4), and internal olefin sulfonate with a distribution of 20–24 carbon atoms (C_{20-24} IOS), were obtained from Stepan Chemical Company. Phenol-2EO, was provided by Harcros Chemicals. This surfactant combination was selected because it shows ideal Winsor type phase behavior with the selected oil and brine at 24 °C and 1 atm. Sodium chloride was purchased from Fisher Scientific with 99.9% purity. The density of brine at 44000 ppm was measured to be 1.026 g/cm^3.

2.2. Brine-oil-surfactant phase behavior and microemulsion viscosity

To characterize Winsor-type phase behavior, desired amounts of water, surfactant, and cosolvent were weighed in glass ampoules and thoroughly mixed using a vortex centrifuge to attain homogeneity. Oil was then added, and ampoules were sealed. Samples were gently mixed and incubated at 24 °C. The surfactant mixture contained TDA and IOS with a fixed mass ratio of 2.75:1 (0.55 wt% TDS, 0.2 wt% IOS) and 1 wt % Phenol-2EO as cosolvent. The phase boundaries were determined with increasing brine salinity. From the equilibrated system, the number and appearance of the phases were determined. The volume levels were recorded and used to calculate the solubilization ratio, defined as the ratio of oil and brine volume to the surfactant volume in the microemulsion phase. Interfacial tensions were estimated using the Huh equation [31].

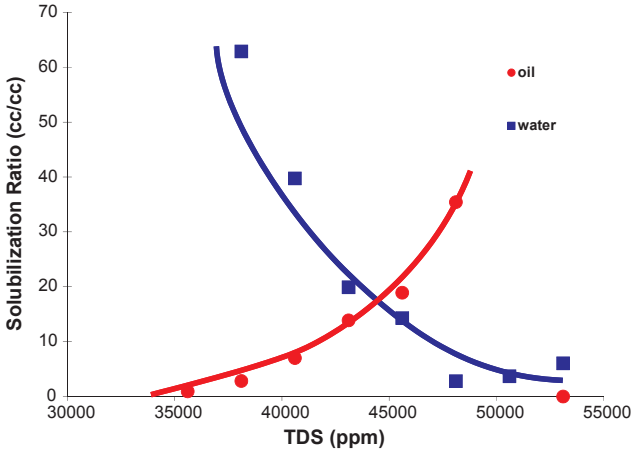

Fig. 1. Solubilization ratios versus salinity plot for 30% oil volume phase behavior experiments. The optimum salinity is at 44,500 ppm TDS.

Fig. 1 shows the solubilization ratios with 30% oil volume and 70% surfactant solution volume. The surfactant-oil system showed favorable phase behavior as the solubilization ratio was greater than 10 (which corresponds to ultra-low IFT by the Huh equation) over a large range of salinities (41,000 ppm TDS salinity to 47,000 ppm TDS). The oil–water crossover point occurs at 44,500 ppm TDS where the solubilization ratio is 18. This is the optimum salinity where IFT is the lowest between oil-microemulsion and water-microemulsion, calculated to be ~10^{-3} mN/m by the Huh equation:

$$\sigma = \frac{C}{\gamma^2} \tag{1}$$

where γ is the solubilization ratio, σ is the interfacial tension and C is a parameter which depends on the surfactant distribution and the structure of the micellar phase [31]. We used the commonly accepted value of C = 0.3 which is appropriate for crude oils and has been validated analytically [32]. All displacement experiments were performed at salinities lower than 50,000 ppm TDS.

The steady-shear rheological measurements were performed on an ARES-LS1 rheometer from TA Instruments, using a double wall couette geometry following Tagavifar's procedure [33]. Fig. 2a shows an example of the viscosity versus shear rate for microemulsion at 47,000 ppm TDS. The microemulsion viscosity is Newtonian up to a shear rate of 100 reciprocal seconds for the entire salinity range. Fig. 2b shows the effect of salinity on microemulsion viscosity. Microemulsion viscosities were measured at 10 reciprocal seconds. The viscosity of the microemulsion increases with salinity up to 50,000 ppm TDS, and after 50,000 ppm TDS microemulsion viscosity decreases rapidly with salinity. This viscosity behavior reflects the microemulsion phase behavior transition from Winsor Type-I to Type-III to Type-II phase environment.

2.3. Micromodel design and fabrication

Photomasks were designed using commercially available vector software, AutoCAD. Transparent film masks (25,400 dpi, with a maximum guaranteed resolution of 10 μm) were ordered from a high-resolution printing company (Cad Art Services). The pore-network was designed using the method developed by Xu et al. [34] to include variations in height at the pore throats which has been successfully used to study different multi-phase flows in porous media [20,35,36]. The pore network array was homogeneous. The pore bodies were ~23 μm deep and the pore throats ~5 μm deep (Fig. 3). The patterns were etched on soda lime glass using standard photolithography procedures and the micromodels were made oil-wet by coating the surface with

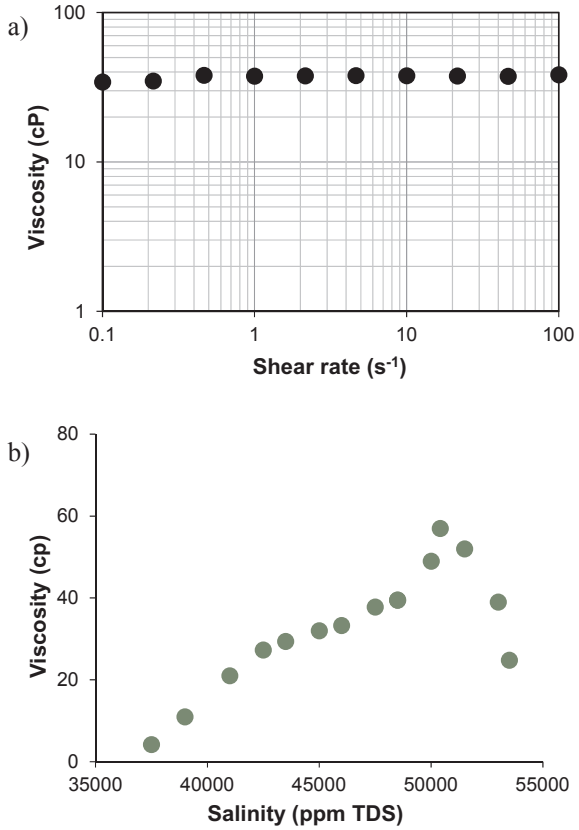

Fig. 2. (a) Example of microemulsion viscosity versus shear rate at 47,000 ppm salinity and (b) microemulsion viscosity versus salinity. Microemulsion viscosities were measured at 10 reciprocal seconds.

chloro-dimethyloctylsilane [37]. Depths were measured using a Dektak 6 M profilometer.

2.4. Apparatus

Fig. 4a shows the design for imbibition experiments where gravity effects were minimized by placing a micromodel horizontally on a flat surface so that the hydrostatic head depended on a 23 μm height. These experiments were performed by submerging 0.7 cm by 3.3 cm micromodels in a sealed vessel in either brine or surfactant solution. Micromodels in these experiments only had one boundary (fracture) open to flow. Images were captured from the top view. In the second set-up (Fig. 4b), the micromodel was placed vertically to include gravity effects. The micromodels used in these experiments were 5 cm by 2.5 cm; two of them had all boundaries open to flow and one of them had three boundaries open to flow. The bottom was sealed to compare results to the experiments and model reported by Li et al. [7]. Images were captured from the side view. In the third design (Fig. 4c) fluids were injected directly into the fracture of a micromodel that rested horizontally (to minimize gravity forces). The micromodel had one inlet and one outlet connected by a single fracture. The fracture was etched using a high-power CO_2 laser and its depth was measured to be 130 μm (Fig. S3 in the supplementary information). No distributors were used to ensure all the oil recovery was due to transverse flow. Images were captured from the top view. All experiments were conducted at 24 °C and 1 atm.

2.5. Experimental parameters and Image acquisition

Static spontaneous imbibition experiments were conducted in the apparatuses shown in Fig. 4a and b. Micromodels were submerged in baths of brine or surfactant solution and images were captured using a single lens reflection (SLR) digital camera (Nikon D5600). Images were taken every 24 h for the static experiments with negligible gravity forces and every ten or fifteen minutes for the gravity driven imbibition experiments. Dynamic experiments were conducted by injecting fluid into micromodels using a Harvard Apparatus PHD 2000 syringe pump,

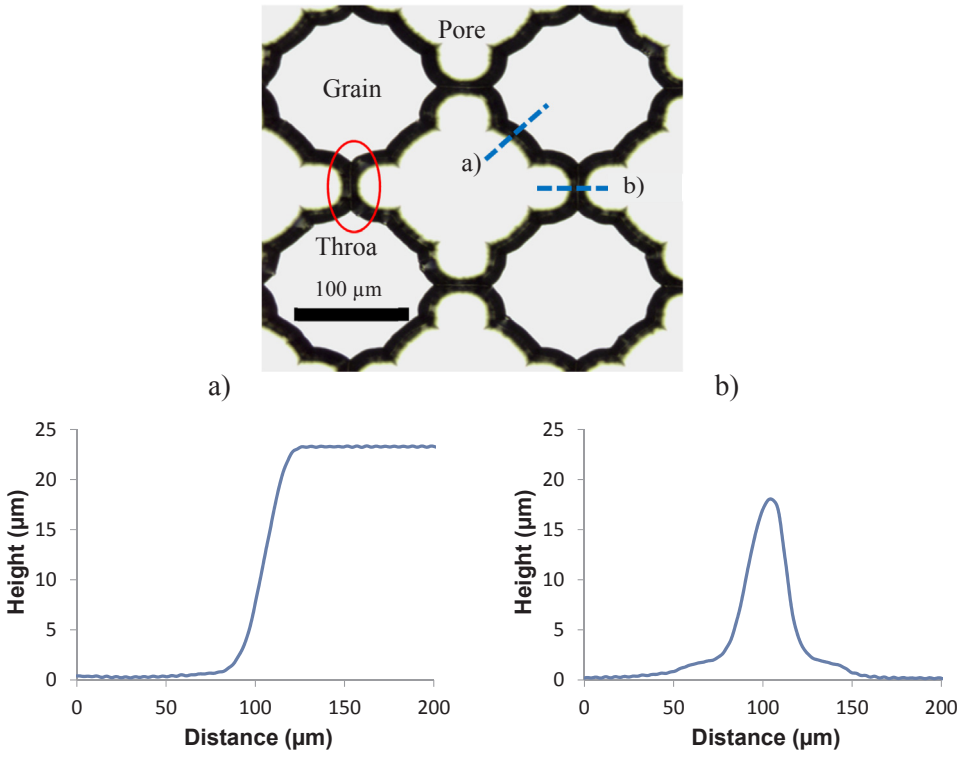

Fig. 3. Micromodel structure measured by an optical profilometer showing (a) pore bodies and (b) pore throats. The pore bodies are approximately 23 μm deep and the pore throats are approximately 1–3 μm deep. The array is homogeneous, so all pore bodies and throats are approximately the same. A pore throat is circled in red. (For interpretation of the references to color in this figure legend, the reader is referred to the web version of this article.)

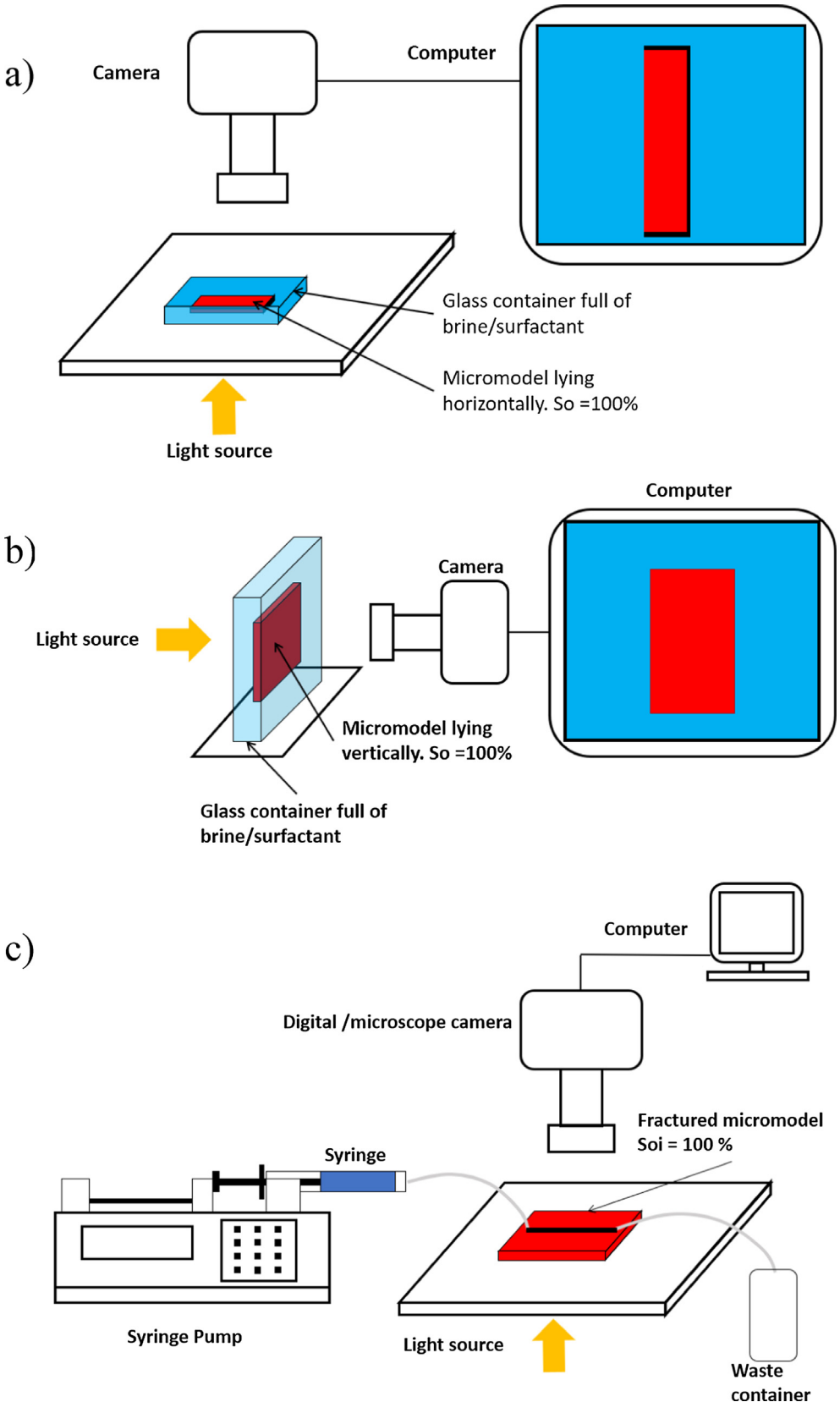

Fig. 4. Experimental set-ups for spontaneous and imposed-flow imbibition experiments. a) static spontaneous experiment with a horizontal micromodel to minimize gravity effects. Only one micromodel side is open to imbibition and the micromodel has one pore in Z-direction. b) static spontaneous imbibition experiment with a vertical micromodel to emphasize the role of gravity. All micromodel sides are open to flow and the micromodel has one pore in Y-direction. c) fractured micromodel used in flooding experiments with minimal gravity effects. The injection is directly into the fracture to minimize the flooding of the porous medium by the imposed flow. The micromodel sides parallel to flow-direction (i.e. left to right in the schematic) are closed boundaries.

Hamilton gas-tight glass syringes (500 μm), and hermetic connections and tubing (IDEx One-Piece Fingertight Fitting, Luer Adapter, Flangeless Ferrule, PEEK Flangeless Headless Short Nut, FEP Tubing accessories). Entire-domain images of dynamic experiments were captured every 5 min using a Nikon D5600 camera at 24.2 MP (pixel size ~20 μm). Microscope images showing multiphase flow at the pore-scale (pixel size ~1 μm) were captured at 60 frames per second using a refraction microscope (Accu-Scope EXI-310) connected to a microscope

camera (Lumera Infinity 3). Fluids were injected at a Darcy velocity of approximately 2 ft/day.

2.6. Image analysis

We used ImageJ for segmentation and processing of the images. Image stacks were converted to 8-bit and thresholded using the Otsu method. We calculated the sensitivity of the segmentation by adjusting the threshold value to ± 5% of the pixel intensity range in each image to ensure segmentation robustness. Finally, grains were accounted for by filtering the images using maximum and minimum grayscale erosion with a pixel radius of five. Oil saturations were calculated by dividing the number of pixels in the oil area by the total number pixels in the image. This segmentation procedure assumes any pixel with a gray scale intensity value greater than that determined by the Otsu method is saturated with oil and any pixel with a value of gray scale intensity lower is brine or microemulsion. This assumption is valid if the volume of microemulsion compared to the oil and brine volumes is small (which our microscopic images confirm), and its effect is captured in the sensitivity calculations (supplementary materials).

3. Results and discussion

3.1. Spontaneous imbibition experiments with negligible gravity effects

A completely oil-saturated, horizontally positioned micromodel was submerged in sodium chloride solution (44,000 ppm TDS) without surfactant. The micromodel was 0.7 cm wide by 3.3 cm long, and had three sealed boundaries and one open boundary. The open boundary had an aperture (glass-etching depth) of 23 μm at the pore bodies, i.e. the maximum height of a fluid column was 23 μm. No oil recovery was observed after the micromodel soaked in brine for 31 days. This is expected as (i) the micromodel glass surface was very oil-wet, (ii) solubility of oil in brine is very low (see supplemental materials), and (iii) the calculated inverse Bond number (N_B^{-1}) is 1.5×10^5, confirming a capillary-dominated imbibition regime [38,39] and negligible gravity impacts. The N_B^{-1} is the ratio of capillary-to-gravity forces and is calculated by

$$N_B^{-1} = \frac{C\sigma\sqrt{\phi/k}}{\Delta\rho g H} \quad (2)$$

where C (=0.4) is a constant, σ(=15 mN/m) is interfacial tension, ϕ (=0.55) denotes void fraction, k (=850 mD – See Supporting Information) is the permeability of porous medium, $\Delta\rho$(=146 kg/m^3) is oil-water density difference, and H(=23 μm) is the height of porous medium exposed to imbibition. Imbibition is capillary-dominated when ${N_B}^{-1} > 5$, gravity-dominated when ${N_B}^{-1} < 0.2$, in the transition regime between the two [38,39].

Introducing surfactant into the system resulted in water imbibition and oil recovery. The surfactant solution salinity was set at the optimum salinity of 44,000 ppm TDS. Nearly half (60%) of the oil was recovered after 31 days of soaking in surfactant solution (Fig. 5). The advancing water front was mostly uniform across the micromodel length after the 31 days of soaking. Some oil ganglia remained, possibly due to non-connectedness of the 2.5D pore-throat features (caused by glass imperfections) that blocked diffusion of micelles into the brine phase or viscous emulsions that formed as the oil–water-surfactant system reached equilibrium. With surfactant decreasing the IFT to 1.2×10^{-3} mN/m, the ${N_B}^{-1}$ is 11.5, suggesting minimal gravity impacts. Table 1 lists the inverse Bond number for all cases studied here.

Since gravitational forces were very small, no applied external forces were applied, and capillary forces were very small the likely mechanism for recovery in this experiment was diffusion of solubilized oil. Once micelles formed (provided their diameter was smaller than the pore throat depth, ~5 μm) they could diffuse across the pore throats. Additionally, previous modeling work showed diffusion is likely the main mechanism for oil mobilization by surfactant solution during unforced imbibition in a hydrophobic capillary filled with oil [23]. To confirm this was the mechanism for oil desaturation, we calculated the advance of the solubilization front using the solubilization rate of n-decane in sodium dodecyl sulfate (SDS) solution at 27 °C measured by Todorov et al. [37] and his observation that the radius of an n-decane sphere solubilized by surfactant decreases linearly:

$$R = -\left(\frac{dR}{dt}\right)t = 1.21\frac{nm}{s}(2,\ 592,\ 000s)\left(\frac{1cm}{1 \times 10^7 nm}\right) = 0.31cm$$

where R is the decrease of an oil droplet radius in surfactant solution, $\frac{dR}{dt}$ is the measured oil solubilization rate, and t is time. To estimate R, we used Todorov's measured solubilization rate for SDS of 1.21 $\frac{nm}{s}$. The calculated R, 0.31 cm, is in the same order as observed value of ~0.4 cm. Given that micelles in type III microemulsions have diameters in the order of ~1–50 nm^2, they should be able to flow across ~5 μm pore throats.

3.2. Gravity-driven spontaneous imbibition experiments

A micromodel with all its boundaries open to flow was positioned vertically in a bath of brine at 44,000 ppm TDS NaCl using the set-up shown in Fig. 4b. Some oil was recovered even in the absence of surfactant. Most of the displacement occurred vertically as brine displaced oil from the bottom where the water-oil pressure difference is highest. After 15 h, oil was recovered from the sides of the micromodel (shown by the small aggregations of blue on the left and right of Fig. 6b). Approximately 3.3% of the initial oil was recovered after 45 h of soaking.

The introduction of a hydrostatic head of 5 cm height allows for some oil to flow upwards by buoyancy. However, the capillary pressure is still two orders of magnitude larger than the pressure difference created by a hydrostatic column of water 5 cm tall:

$$P_c = \frac{2\sigma\cos\theta}{r} = \frac{2\left(35\frac{mN}{m}\right)\cos 180°}{1\mu m} = -7 \times 10^4 Pa = -10psi$$

$$\Delta P = \Delta\rho g h = \left(146\frac{kg}{m^3}\right)\left(9.81\frac{m}{s^2}\right)(0.05m) = 72.6Pa = 0.011psi$$

Therefore, very little desaturation should occur. The high inverse Bond number of 67.8 (see Table 1) also supports this assertion.

To investigate low-IFT imbibition, another experiment was conducted with the same geometry and boundary conditions (all boundaries open to flow) but with surfactant solution at the optimum salinity (44,000 ppm TDS) surrounding the micromodel. The presence of surfactant resulted in a marked increase in the rate of oil recovery (Fig. 7). For a micromodel immersed in surfactant solution, 30% of the oil was recovered after two and a half hours. The oil was displaced mostly vertically but also from the sides (as can be seen after 5.3 h of soaking where the oil is almost completely disconnected from the micromodel's side boundaries). After 7.9 h of immersion, more than half of the oil (74%) was recovered. Some streaks of oil remained in the water-invaded region of the micromodel after 7.9 h. This oil stayed in place possibly due to an accumulation of viscous emulsions that hindered flow. Most of the streaks have an orientation that is indicative of the flow direction; residual streaks appear thin and elongated mostly vertically but with a horizontal component.

An order of magnitude force balance calculation with the introduction of surfactant at ultra-low IFT shows desaturation can occur as buoyant forces are larger than capillary forces:

$$P_c = \frac{2\sigma\cos\theta}{r} = \frac{2\left(1.2 \times 10^{-3}\frac{mN}{m}\right)\cos 180°}{1\mu m} = -2Pa = -3 \times 10^{-4}psi$$

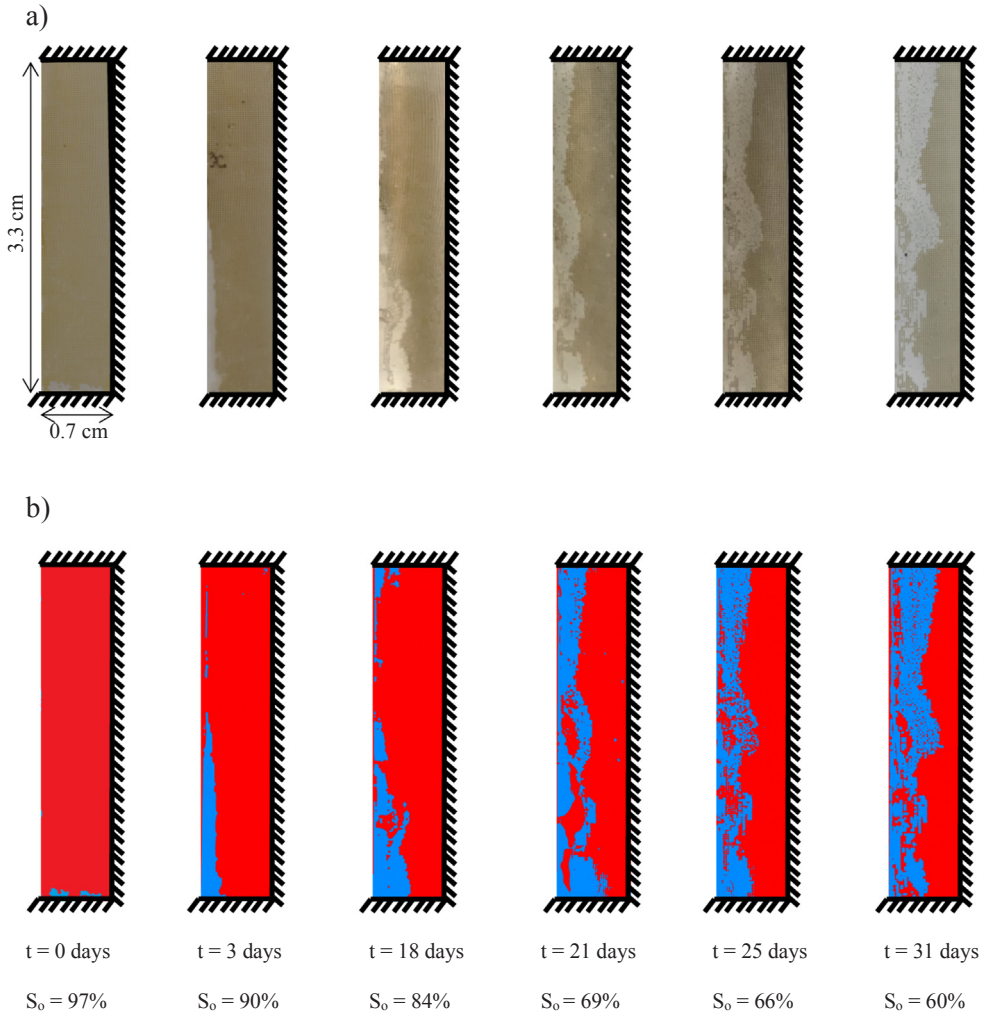

Fig. 5. Image sequence of micromodel soaking in surfactant solution. Approximately 40% is recovered after 31 days. Sequence (a) shows the original photographs, while (b) shows the segmented and colored images. The recovery front is mostly uniform; however, some blobs of oil remain in the aqueous solution-saturated region of the micromodel. Images were binarized and oil saturated regions were colored red while brine or surfactant solution-saturated regions were colored blue. The rest of the images in this work are presented with the same color legend. (For interpretation of the references to color in this figure legend, the reader is referred to the web version of this article.)

Table 1
Inverse Bond number for spontaneous imbibition cases with and without surfactant. The height of micromodel is 5 cm for the vertical case and 23 μm (i.e. height of the pore) in the horizontal one.

Case	σ/H(N/m^2)	N_B^{-1}
Vertical micromodel-Brine	0.3	67.8
Vertical micromodel-Surfactant	2.3×10^{-5}	0.005
Horizontal micromodel-Brine	652.2	1.5×10^5
Horizontal micromodel-Surfactant	0.05	11.5

$$\Delta P = \Delta\rho g h = \left(146\frac{kg}{m^3}\right)\left(9.81\frac{m}{s^2}\right)(0.05m) = 72.6Pa = 0.011psi$$

The introduction of surfactant reduces the capillary forces to a value two orders of magnitude lower than the pressure head from the water column. For this calculation we assume a contact angle of 180° to be as conservative as possible in the estimation of capillary forces holding the oil in place.

Worth noting is the change in sweep stability from 2.6 h to 5.3 h. At 2.6 h the oil is displaced somewhat evenly from the bottom, while at 5.3 h there are visible instabilities at the oil-surfactant solution interface. Through simulation studies, Tagavifar et al. [40] showed a weak viscous instability occurs in low-IFT spontaneous imbibition since upstream of the optimum microemulsion lie the less-viscous microemulsions and the surfactant solution. Berg and Ott elaborate on the development of viscous instabilities and their occurrences at different scales, including the centimeter scale [41]. Viscous instabilities in ASP processes have been visualized at the core scale using CT imaging [42], and in micromodels in heavy oil displacements [43]. However, these experiments did not include fractures and the viscosity contrast (13 cp oil versus 1 cp brine) was not as marked as in heavy oil displacements where oil is usually several orders of magnitude more viscous than the brine. Our experiment suggests viscous instabilities can occur at the centimeter scale in the presence of fractures.

3.3. Comparison with analytical imbibition scaling model

A micromodel's bottom boundary was sealed using 5-minute epoxy and the micromodel was immersed in surfactant solution at optimum salinity (44,000 ppm TDS) (Fig. 8). The purpose of this experiment was to visualize and evaluate gravity-dominated spontaneous imbibition in a vertical micromodel with closed-bottom boundary condition and compare the results with those reported by Li et al. [7] with cylindrical core plugs submerged in surfactant solution where invasion of the surfactant solution was limited to the top and sides. They proposed the following scaling model for gravity-dominated spontaneous imbibition:

$$t_D = \frac{2kk_{\mu E}\Delta\rho g H t}{\phi\mu_{\mu E}(R^2 + MH^2)} \tag{3}$$

$$\frac{\Delta V_o}{V_{oi}} = \sqrt{t_D} - \frac{t_D}{3} \tag{4}$$

where t_D is dimensionless time, k is absolute permeability, $k_{\mu E}$ is microemulsion relative permeability, $\Delta\rho$ is the fluid density difference, H

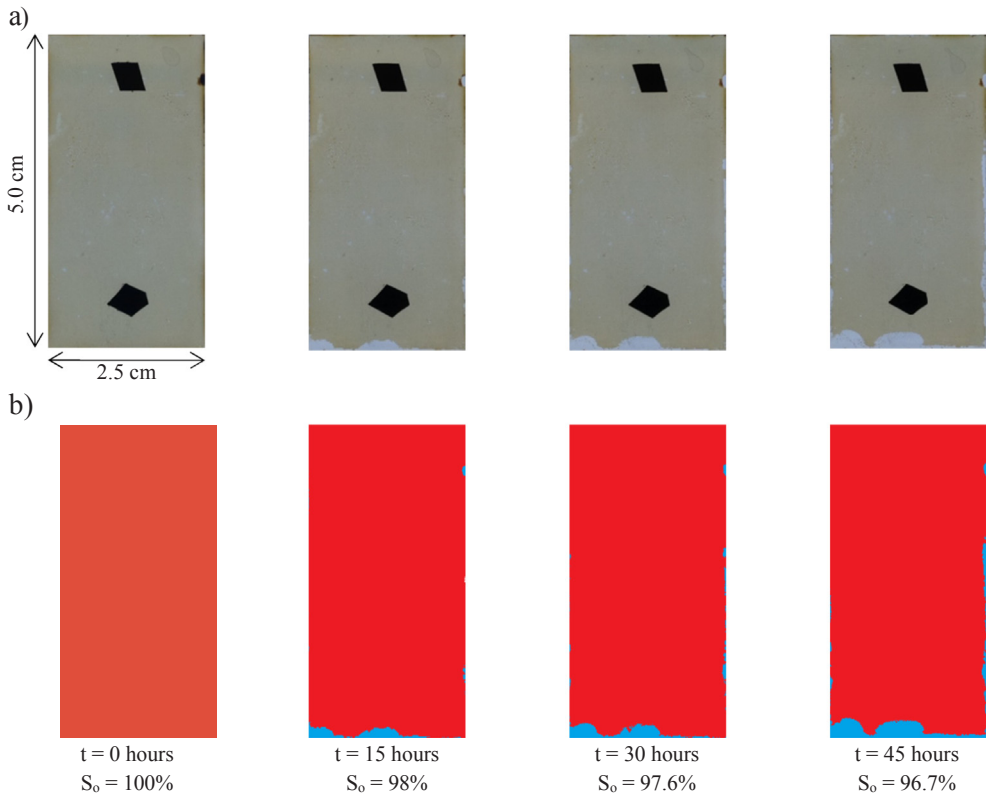

Fig. 6. Micromodel standing vertically in a brine bath at 44,000 ppm TDS sodium chloride. Sequence (a) shows the original photographs, while (b) shows the segmented and colored images. All boundaries are open to flow. The black polygons in the original images are pieces of electrical tape that cover the injection ports.

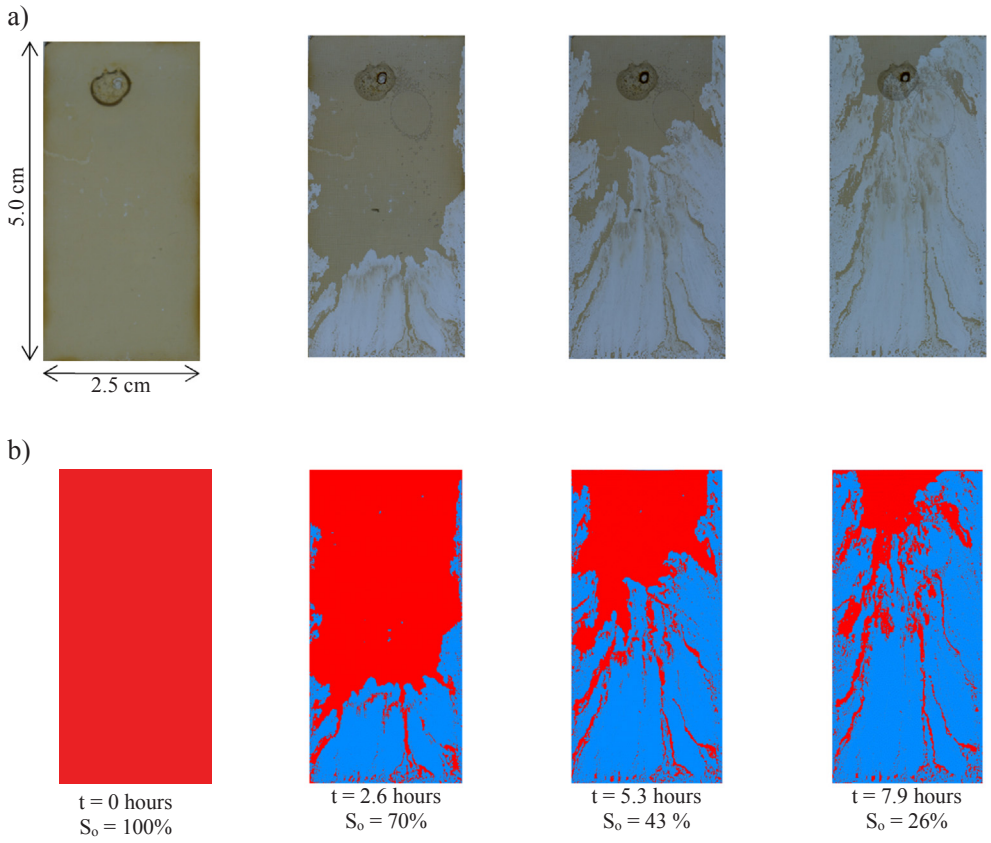

Fig. 7. Image sequence of oil recovery in a vertically positioned micromodel submerged in surfactant solution at the optimum salinity, 44,000 ppm TDS. All boundaries are open to flow. Sequence (a) shows the original photographs, while (b) shows the segmented and colored images. Approximately 75% of the oil was recovered from the micromodel after eight hours.

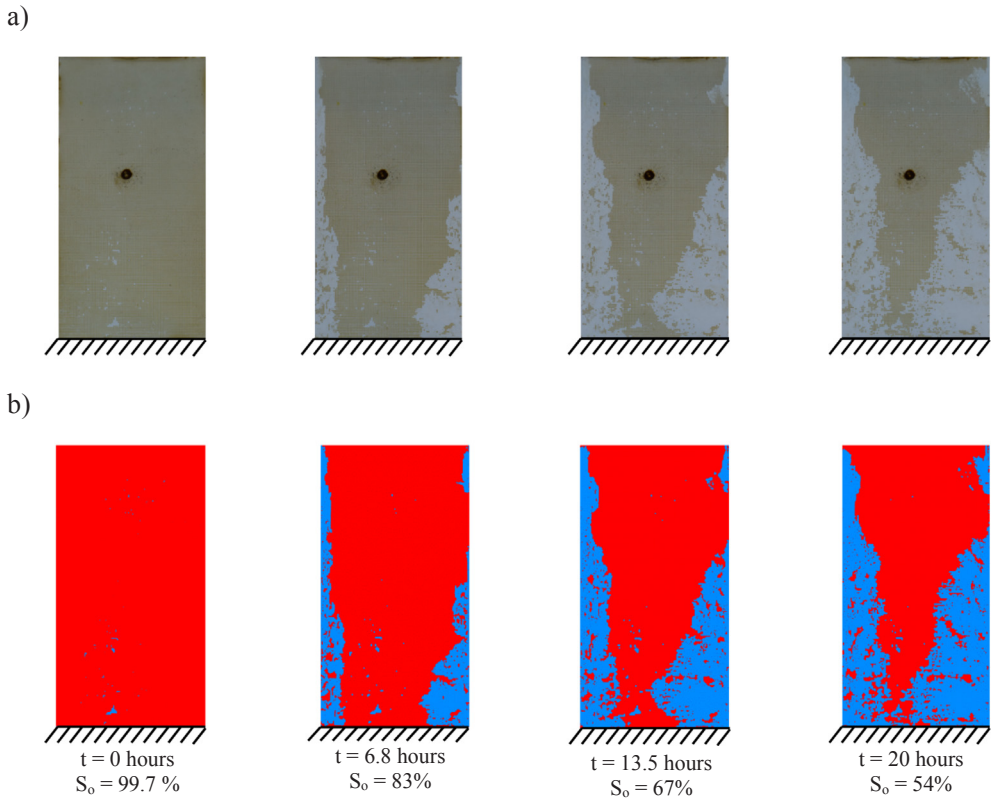

Fig. 8. Image sequence of oil recovery over time in a vertically positioned micromodel with a sealed bottom. Sequence (a) shows the original photographs, while (b) shows the segmented and colored images.

is the core's height, g is the gravitational constant, t is time, ϕ is porosity, $\mu_{\mu E}$ is microemulsion viscosity, R is the core's radius and M is the mobility ratio of microemulsion to oil. This model assumes low IFT, conical displacement pattern, uniform permeability, porosity, initial oil saturation, incompressible fluids, local equilibrium for microemulsion generation, and uniform adsorption. Of these, local equilibrium and uniform adsorption cannot be verified in this micromodel.

Fig. 8 shows the imbibition process over time. As seen, the recovery pattern appears conical. The top boundary remained completely saturated with oil while the bottom boundary was swept from the sides. Some oil ganglia were unswept but it is notable that their shape was different from those in the experiment shown in Fig. 7. Remaining ganglia in this experiment do not show clear elongation in the vertical direction.

Fig. 9 compares our experimental results of oil saturation versus time with that calculated using the scaling model (Eq. (4)). The fitting was done by adjusting the oil and microemulsion relative permeability to, respectively, 0.4 and 0.3. These values are similar to those estimated by Li et al. [7] in some of their experiments. Except for the first 10 h, the model fitted the experimental data quite well. We speculate the mismatch at early time is due to the remaining oil ganglia in the surfactant solution invaded region. The model assumes all the oil in this region is swept, but this is not the case for this experiment. Furthermore, although the oil-saturated region is approximately conical, some asymmetry is noticeable as the right side of the cone is less well defined.

To further highlight the role of imbibition and boundary conditions, Fig. 10 compares the three previous experiments in the vertical

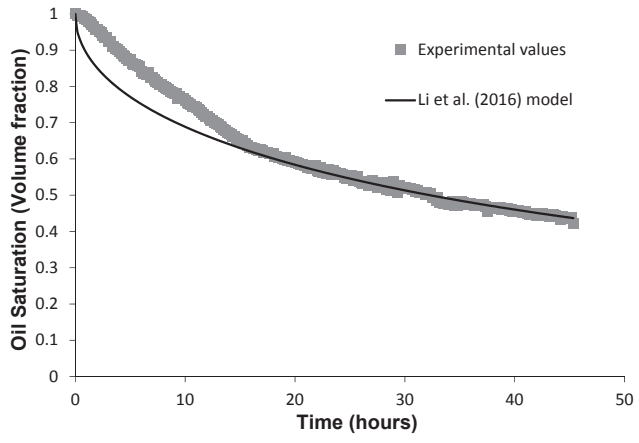

Fig. 9. Plot of oil saturation versus time for vertically positioned micromodel with a closed bottom boundary and scaling imbibition model by Li et al. (2016). Fitted variables were $k_{\mu E} = 0.3$ and $k_o = 0.4$. Other inputs to the scaling equation were k = 1D, $\Delta\rho = 146\ kg/m^3$, H = 5.0 cm, R = 2.5 cm, $\phi = 0.506$, $g = 9.8\ m/s^2$, $\mu_{\mu E} = 30cp$.

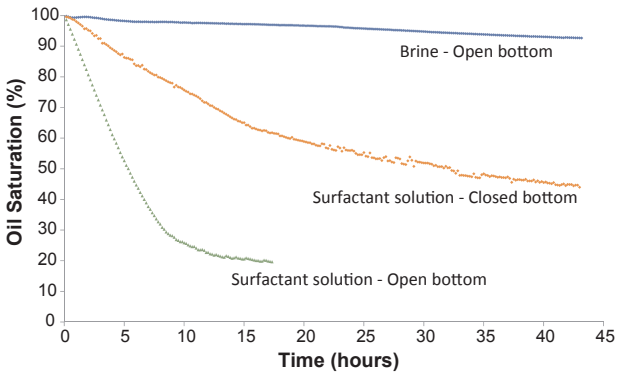

Fig. 10. Comparison of oil recovery versus time for vertically positioned micromodels undergoing spontaneous imbibition.

micromodel. The brine imbibition experiment (i.e. no surfactant) with all-open boundaries recovered less than 4% oil after two days. Using surfactant with the same all-open boundaries (the green curve in Fig. 10) shows a significant decrease in oil saturation in the first ten hours of immersion. After about ten hours, the oil saturation decreases slowly. The case where the micromodel's bottom boundary is sealed (orange curve in Fig. 10) shows considerably slower recovery compared to the all-open boundaries. The slower recovery with closed-bottom boundary arises from (i) decreasing contact area between the porous medium and surfactant solution and (ii) lack of relative permeability transition to ultra-low IFT regime where k_r scales linearly with phase saturation [43].

3.4. Experiments with imposed flow

Injection experiments were conducted using the fractured porous medium setup shown in Fig. 4c. Micromodels were placed horizontally on a flat surface to minimize gravity effects and images were taken with a digital camera or optical microscope. We injected directly into the fracture to eliminate longitudinal flow across the matrix. The fracture depth and width were measured to be 130 μm and 1000 μm respectively (See Supporting Information). Fracture permeability (1500 D) was calculated using the fracture dimensions and equating Bussinesq's equation for laminar flow in a rectangular cross section to Darcy's law. Matrix permeability (0.85 D) was calculated inputting measured pressure drops at steady state across a non-fractured micromodel into Darcy's law. The calculations and fracture dimensions are included in the supporting information. The fracture-to-matrix permeability ratio was ~1765.

Injecting brine into the fracture of a completely oil-saturated micromodel resulted in the displacement of oil from the fracture. After 100 h of brine injection, no oil from the matrix was recovered (first image in the sequence of Fig. 11). No oil was recovered from the matrix because it was oil-wet, and the fracture was > 1000 times more permeable than the matrix.

Injecting surfactant solution at the optimum salinity, 44,000 ppm TDS, after the waterflood resulted in oil recovery from the matrix (Fig. 11). The surfactant was injected at 3.2 μL/min, equivalent to a velocity of 7×10^{-6} *m/s* (or 2 *ft/day*) in the fracture. Approximately 25% of the oil is recovered after one hour of flooding. The time dependence of oil recovery is in the same order as surfactant gravity driven imbibition (Fig. 10). However, in this experiment fewer residual streaks were observed than in the gravity driven imbibition experiments.

Microscopic images of the boundary between surfactant solution and oil of an ongoing surfactant flood (Fig. 12) shows details of multiphase flow at low IFT; pore filling events are not very fast, and pores are partially filled by different fluids. Three phases are present in some individual pores: the oil is dark brown, the brine is clear, and the microemulsion is light brown. Additionally, flow of oil and microemulsion occurs in bridges and films as observed by Jamaloei and Kharrat (2009).

The microemulsion phase has interfaces with both the aqueous and the oleic phases, and its color ranges between the oil (dark brown) and the aqueous solution (clear). Fig. 12 shows there is a gradient in color in some of the pores as microemulsion begins to form but there is no visible interphase between it and the oil. The oleic phase looks dark brown and light brown in the same pore while no interface is present. Also notable is the presence of emulsion bubbles in some of the pores (especially visible in Fig. 12 in one of the central pores that is disconnected from the pore below it and the pore to its left). In this pore, bubbles aggregate on the disconnected dead-end crevice.

During surfactant injection, wettability is not as clearly defined as in the original oil-wet state. While IFT reduction and microemulsion

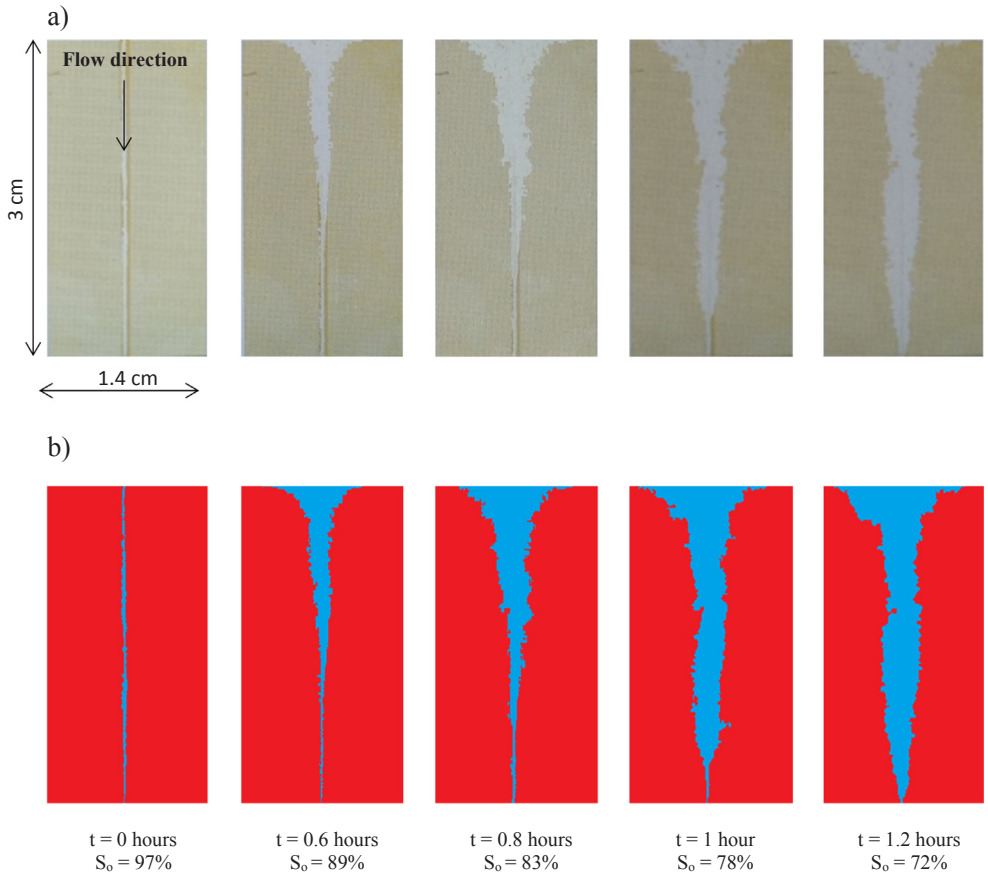

Fig. 11. Image sequence of oil saturation over time in a fractured micromodel undergoing aqueous surfactant injection. Sequence (a) shows the original photographs, while (b) shows the segmented and colored images. The recovery pattern is approximately conical and all recovery is due to crossflow of oil from the matrix to the fracture.

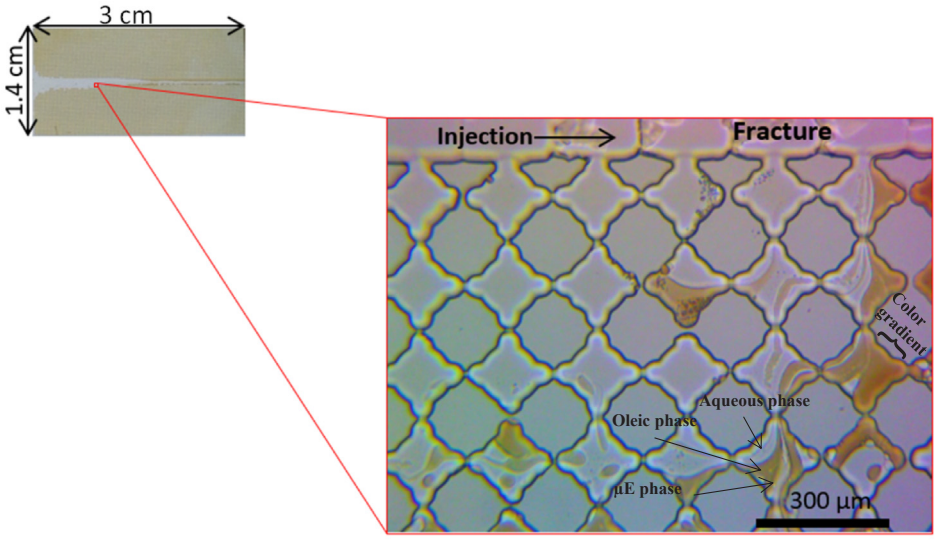

Fig. 12. Micro-view of oil-aqueous solution-microemulsion multiphase flow in micromodel porous medium. Surfactant solution is directly injected into the fracture (seen at the top of the image), and flows into the matrix by viscous crossflow. Oil is dark brown and microemulsion is light-yellow. (For interpretation of the references to color in this figure legend, the reader is referred to the web version of this article.)

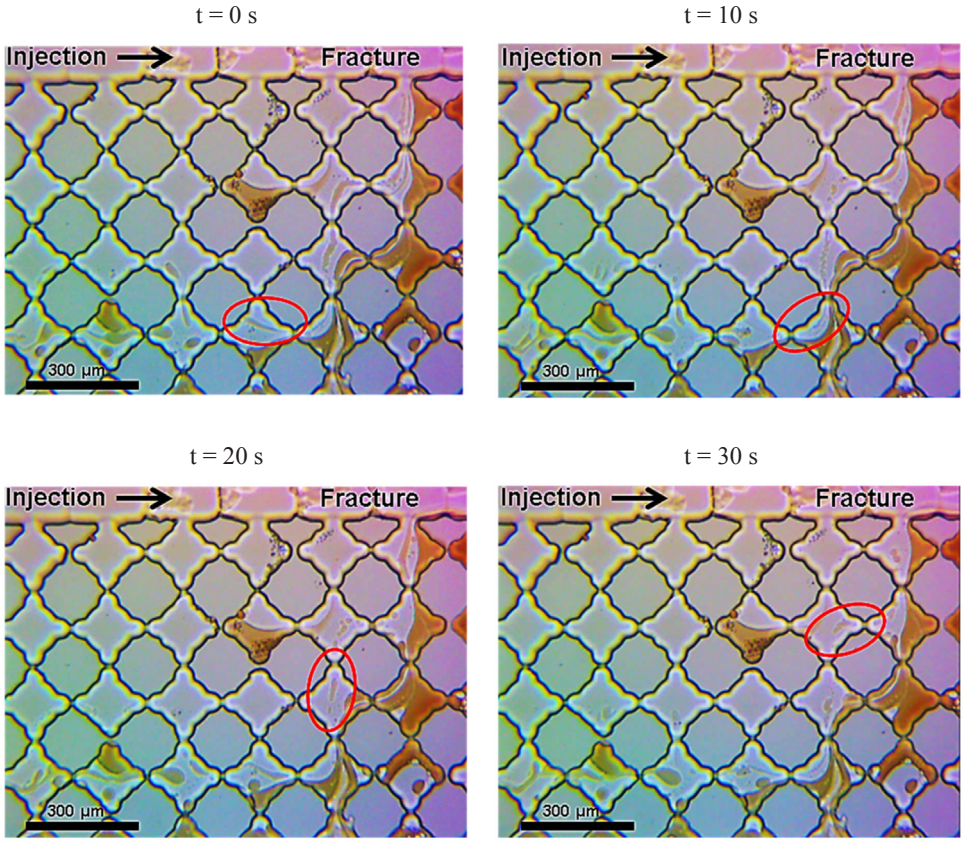

Fig. 13. Image sequence highlighting crossflow of microemulsion from the matrix into the fracture.

formation are fast, the wettability change is comparatively slow and has non-uniform & non-equilibrium characteristics. Fig. 12 shows that during the flood some pores are preferentially wetted by oil, some by water, some by microemulsion and some by combinations of two or three of the phases (where contact angles are close to 90°). Given enough time, the wettability is altered from the initial oil-wet state to a mixed-wet state and finally to an aqueous surfactant wettability [20].

The flow of oil or microemulsion can be tracked in this system if a disconnected bubble flows from the matrix to the fracture. Fig. 13 highlights an isolated ganglion of microemulsion that flows in the direction transverse to injection. Since gravity forces are negligible and there are no flow distributors imposing a pressure drop across the matrix, the movement of these ganglia must be due to transverse pressure gradients.

The microemulsion ganglion highlighted in Fig. 13 decreases in size as it moves from the matrix into the fracture. Some of the micelles diffuse from the microemulsion ganglion to the brine as the ganglion moves through the network and is sheared by the convergent-divergent geometry both in the areal plane and in the direction perpendicular to the areal plane (because the pore throats are shallower than the pore bodies). Any oil removed from the matrix should result in water flowing into the matrix because oil and water have very low compressibility at

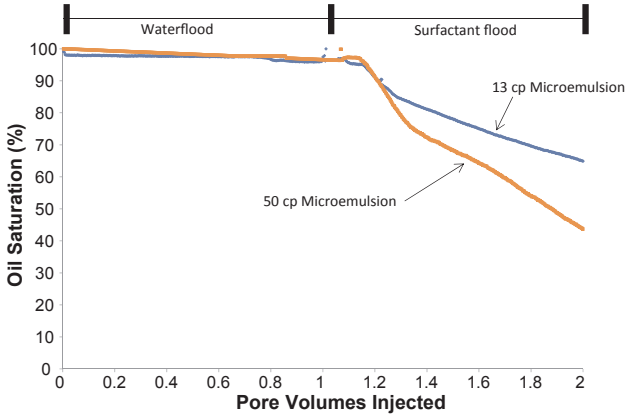

Fig. 14. The effect of microemulsion viscosity on oil recovery in oil-wet fractured micromodels in the same geometry.

room temperature and pressure. We observed the movement of isolated water into the oil at another section of the micromodel (Fig. S7 in the supporting information).

3.5. Effect of microemulsion viscosity on oil recovery

Fig. 14 presents the effect of microemulsion viscosity on oil recovery. Previous core-flood experiments showed that flowing a more viscous microemulsion through the fracture produces oil faster from the matrix because the transverse pressure gradients are higher [10]. We tested the hypothesis in our system and obtained results that agree with their observations. Injecting surfactant solution at higher salinity (that produces a more viscous microemulsion) resulted in faster recovery from the fractured micromodels.

4. Conclusions

- A micromodel with a transverse fracture was fabricated to study mechanisms of surfactant flooding in oil-wet fractured porous media. To disentangle the effects of viscous forces, gravity, and IFT reduction (solubilization), and to determine the time scales of recovery by each mechanism, we conducted spontaneous imbibition as well as flooding experiments.
- Spontaneous imbibition experiments in imbibition cells with minimal gravity effects ($N_B^{-1} > 10^5$) showed that 40% of the oil can be recovered by IFT reduction/solubilization in 31 days. Results with low-IFT and gravity effects (N_B^{-1} 0.005) showed that gravity speeds up the recovery by ~20 times (for similar boundary conditions) and results in additional oil recovery (20% extra oil here). However, the recovery depended on boundary condition as well as recovery mechanism, where the highest and fastest recovery (80% oil recovery in 0.6 days) was obtained with the all-open boundary condition.
- Oil desaturation in dynamic experiments, where surfactant solution was injected directly into the fracture, occurred because of transverse pressure gradients and solubilization. The viscous crossflow resulted in ~40% oil recovery in 3–4 h with frontal velocity of 2 ft/day in fracture. Oil and microemulsion ganglia were observed flowing in the bulk brine phase from the matrix into the fracture. Recovery increased as the viscosity of the microemulsion increased, suggesting higher viscosity microemulsion generates larger transverse viscous pressure gradients.
- Microscopic images of dynamic experiments showed while IFT reduction and microemulsion formation are fast, the wettability change is comparatively slow and has non-uniform & non-equilibrium characteristics. These indicate wettability alteration was not the most significant mechanism for oil recovery in our micromodel as (i) the ultralow IFT minimizes the impact of capillary pressures and (ii) the aqueous surfactant solution is not clearly the wetting phase when it enters the matrix. However, the wettability transitions from the initial oil-wet to a mixed-wet state at short times and subsequently to an aqueous surfactant-wet at later times.
- Results from this study suggest mechanisms of surfactant flooding in fractured carbonates have different time-scales. The same amount of oil recovery was observed in weeks with solubilization/IFT reduction, in day(s) with gravity/IFT-reduction, and in hours with viscous crossflow. These results suggest that viscous forces and the mobility-enhancing properties of in-situ generated microemulsions should be considered as a design variable. While wettability alteration and solubilization can recover oil from the matrix, these processes are slow compared to recovery by viscous crossflow or gravity driven displacements.

Acknowledgements

The authors would like to thank the Chemical EOR Industrial Affiliates Project in the Center of Petroleum and Geosystems Engineering at the University of Texas at Austin for financial support.

We would also like to thank Dr. Masa Prodanovic for her valuable advice regarding image processing.

Appendix A. Supplementary data

Supplementary data to this article can be found online at https://doi.org/10.1016/j.fuel.2018.12.076.

References

[1] Bagrintseva KI. Carbonate reservoir rocks. 1st Ed Hoboken, New Jersey: Wiley, Scrivener Publishing; 2015.
[2] Chilingar GV, Yen TF. Some notes on wettability and relative permeabilities of carbonate reservoir rocks, II. Energy Sources 1983;7:67–75. https://doi.org/10.1080/00908318308908076.
[3] Nelson RA. Geologic analysis of naturally fractured reservoirs. 2nd Ed. Houston: Gulf Professional Publishing; 2001.
[4] Standnes DC, Austad T. Wettability alteration in chalk 2. Mechanism for wettability alteration from oil-wet to water-wet using surfactants. J Pet Sci Eng 2000;28:123–43. https://doi.org/10.1016/S0920-4105(00)00084-X.
[5] Hirasaki G, Zhang DL. Surface chemistry of oil recovery from fractured, oil-wet, carbonate formations. SPE J 2004;9:151–62. https://doi.org/10.2118/88365-PA.
[6] Gupta R, Mohanty KK. Wettability alteration mechanism for oil recovery from fractured carbonate rocks. Transp Porous Media 2011;87:635–52. https://doi.org/10.1007/s11242-010-9706-5.
[7] Li Y, Lu J, Churchwell L, Tagavifar M, Weerasooriya U, Pope GA. Scaling of low IFT imbibition in oil-wet carbonates. Tulsa, OK, USA SPE Improved Oil Recovery Conf2016:11–3. https://doi.org/10.2118/179684-MS.
[8] Abbasi Asl Y, Pope GA, Delshad M. Mechanistic modeling of chemical transport in naturally fractured oil reservoirs. Tulsa, OK, USA SPE Improved Oil Recovery Symp2010:24–8. https://doi.org/10.2118/129661-MS.
[9] Lu J, Goudarzi A, Chen P, Kim DH, Delshad M, Mohanty KK, et al. Enhanced oil recovery from high-temperature, high-salinity naturally fractured carbonate reservoirs by surfactant flood. J Pet Sci Eng 2014;124:122–31. https://doi.org/10.1016/j.petrol.2014.10.016.
[10] Parra JE, Pope GA, Mejia M, Balhoff MT. New approach for using surfactants to enhance oil recovery from naturally fractured oil-wet carbonate reservoirs. Dubai, UAE SPE Annu Tech Conf Exhibition2016:26–8. https://doi.org/10.2118/181713-MS.
[11] Wildenschild D, Sheppard AP. X-ray imaging and analysis techniques for quantifying pore-scale structure and processes in subsurface porous medium systems. Adv Water Resour 2013;51:217–46. https://doi.org/10.1016/j.advwatres.2012.07.018.
[12] Cnudde V, Boone MN. High-resolution X-ray computed tomography in geosciences: A review of the current technology and applications. Earth-Sci Rev 2013;123:1–17. https://doi.org/10.1016/j.earscirev.2013.04.003.
[13] Ruecker M, Bartels W-B, Unsal E, Berg S, Brussee N, Coorn A, et al. The formation of microemulsion at flow conditions in rock. Int Symp Soc Core Anal 2017;27. Vienna, Austria.
[14] Karadimitriou NK, Hassanizadeh SM. A review of micromodels and their use in two-phase flow studies. Vadose Zone J 2012;11. https://doi.org/10.2136/vzj2011.0072.
[15] Lifton VA. Microfluidics: an enabling screening technology for enhanced oil recovery (EOR). Lab Chip 2016;16:1777–96. https://doi.org/10.1039/C6LC00318D.
[16] Anbari A, Chien H-T, Datta SS, Deng W, Weitz DA, Fan J. Microfluidic model porous media: fabrication and applications. Small 2018;14:1703575. https://doi.org/10.

1002/smll.201703575.
[17] Oh KW, Lee K, Ahn B, Furlani EP. Design of pressure-driven microfluidic networks using electric circuit analogy. Lab Chip 2012;12:515–45. https://doi.org/10.1039/C2LC20799K.
[18] Conn CA, Ma K, Hirasaki GJ, Lisa Biswal S. Visualizing oil displacement with foam in a microfluidic device with permeability contrast. Lab Chip 2014;14:3968–77. https://doi.org/10.1039/C4LC00620H.
[19] Broens M, Unsal E. Emulsification kinetics during quasi-miscible flow in dead-end pores. Adv Water Resour 2018;113:13–22. https://doi.org/10.1016/j.advwatres.2018.01.001.
[20] Tagavifar M, Xu K, Jang SH, Balhoff MT, Pope GA. Spontaneous and flow-driven interfacial phase change: dynamics of microemulsion formation at the pore scale. Langmuir 2017;33:13077–86. https://doi.org/10.1021/acs.langmuir.7b02856.
[21] Rangel-German ER, Kovscek AR. A micromodel investigation of two-phase matrix-fracture transfer mechanisms: investigation of transfer mechanisms. Water Resour Res 2006;42.. https://doi.org/10.1029/2004WR003918.
[22] Mehmani A, Kelly S, Torres-Verdin C, Balhoff M. Quantification of fracture-matrix fluid transport in unconventional rocks using two-scale microfluidic chips. In: Unconventional Resources Technology Conference, 24–26 July, Austin, TX, USA. doi:10.15530/urtec-2017-2669314.
[23] Hammond PS, Unsal E. Spontaneous and forced imbibition of aqueous wettability altering surfactant olution into an initially oil-wet capillary. Langmuir 2009;25:12591–603. https://doi.org/10.1021/la901781a.
[24] Hammond PS, Unsal E. A dynamic pore network model for oil displacement by wettability-altering surfactant solution. Transp Porous Media 2012;92:789–817. https://doi.org/10.1007/s11242-011-9933-4.
[25] Hornof V, Morrow NR. Flow visualization of the effects of interfacial tension on displacement. SPE Reserv Eng 1988;3:251–6. https://doi.org/10.2118/14930-PA.
[26] Pei H, Zhang G, Ge J, Tang M, Zheng Y. Comparative effectiveness of alkaline flooding and alkaline-surfactant flooding for improved heavy-oil recovery. Energy Fuels 2012;26:2911–9. https://doi.org/10.1021/ef300206u.
[27] Kianinejad A, Ghazanfari MH, Kharrat R, Rashtchian D. An experimental investigation of surfactant flooding as a good candidate for enhancing oil recovery from fractured reservoirs using one-quarter five spot micromodels: the role of fracture geometrical properties. Energy Sources Part Recovery Util Environ Eff 2013;35:1929–38. https://doi.org/10.1080/15567036.2010.525591.
[28] Sedaghat MH, Ghazanfari MH, Masihi M, Rashtchian D. Experimental and numerical investigation of polymer flooding in fractured heavy oil five-spot systems. J Pet Sci Eng 2013;108:370–82. https://doi.org/10.1016/j.petrol.2013.07.001.
[29] Howe AM, Clarke A, Mitchell J, Staniland J, Hawkes LA. Visualising surfactant EOR in core plugs and micromodels, SPE Asia Pacific Enhanced Oil Recovery Conference, 11–13 August, Kuala Lumpur. Malaysia 2015. https://doi.org/10.2118/174643-MS.
[30] Alzahid YA, Peyman M, Walsh SDC, Armstrong RT. Flow regimes during surfactant flooding: the influence of phase behaviour. Fuel 2018:851–60. https://doi.org/10.1016/j.fuel.2018.08.086.
[31] Huh C. Interfacial tensions and solubilizing ability of a microemulsion phase that coexists with oil and brine. J Colloid Interface Sci 1979;71:408–26. https://doi.org/10.1016/0021-9797(79)90249-2.
[32] Ghosh S, Johns RT. Dimensionless equation of state to predict microemulsion phase behavior. Langmuir 2016;32:8969–79. https://doi.org/10.1021/acs.langmuir.6b02666.
[33] Tagavifar M, Herath S, Weerasooriya UP, Sepehrnoori K, Pope G. Measurement of microemulsion viscosity and its implications for chemical enhanced oil recovery. SPE J 2018;23:066–83. https://doi.org/10.2118/179672-PA.
[34] Xu K, Liang T, Zhu P, Qi P, Lu J, Huh C, et al. A 2.5-D glass micromodel for investigation of multi-phase flow in porous media. Lab Chip 2017;17:640–6. https://doi.org/10.1039/C6LC01476C.
[35] Xu K, Bonnecaze R, Balhoff M. Egalitarianism among bubbles in porous media: an ostwald ripening derived anticoarsening phenomenon. Phys Rev Lett 2017:119. https://doi.org/10.1103/PhysRevLett.119.264502.
[36] Du Y, Xu K, Mejia L, Zhu P, Balhoff MT. Multiscale Microfluidic investigation of low salinity effects during oil recovery. Soc Pet Eng J 2019. under review.
[37] Hermanson GT. Chapter 13 – Silane Coupling Agents. Bioconjugate Tech Third Ed.Boston: Academic Press; 2013. p. 535–48. https://doi.org/10.1016/B978-0-12-382239-0.00013-3.
[38] Schechter DS, Zhou D, Orr FM. Low IFT drainage and imbibition. J Pet Sci Eng 1994;11:283–300. https://doi.org/10.1016/0920-4105(94)90047-7.
[39] Zhou D, Jia L, Kamath J, Kovscek AR. Scaling of counter-current imbibition processes in low-permeability porous media. J Pet Sci Eng 2002;33:61–74. https://doi.org/10.1016/S0920-4105(01)00176-0.
[40] Tagavifar M, Balhoff M, Mohanty K, Pope GA. Dynamics of low-IFT imbibition in oil-wet Carbonates. SPE J 2019. Preprint.
[41] Berg S, Ott H. Stability of CO2–brine immiscible displacement. Int J Greenh Gas Control 2012;11:188–203. https://doi.org/10.1016/j.ijggc.2012.07.001.
[42] van Batenburg DW, Berg S, Oedai S, David LL, Siemens AON. Elewaut K. Visualisation of light oil mobilisation in ASP core floods using X-Ray CT Imaging. SPE Asia Pac Enhanc Oil Recovery Conf, Kuala Lumpur, Malaysia: Society of Petroleum Engineers 2015. https://doi.org/10.2118/174660-MS.
[43] Doorwar S, Mohanty KK. Viscous fingering during non-thermal heavy oil recovery. . SPE Annu. Tech. Conf. Exhib., Denver, Colorado, USA: Soc Pet Eng 2011. https://doi.org/10.2118/146841-MS.